Reports on Progress in Physics

PAPER • OPEN ACCESS

Understanding polaronic transport in complex oxides by combining precise synthesis and first-principles many-body theory

To cite this article: Fengdeng Liu *et al* 2026 *Rep. Prog. Phys.* **89** 028003

IOP Publishing Rep. Prog. Phys. **89** (2026) 028003 https://doi.org/10.1088/1361-6633/ae3c3e

Reports on Progress in Physics

Check for updates

OPEN ACCESS

RECEIVED
8 November 2025

REVISED
23 December 2025

ACCEPTED FOR PUBLICATION
22 January 2026

PUBLISHED
23 February 2026

PAPER

Understanding polaronic transport in complex oxides by combining precise synthesis and first-principles many-body theory

Fengdeng Liu[1,2,6], **Zhifei Yang**[1,3,6], **Yao Luo**[4,6], **Silu Guo**[1], **Chi Zhang**[5], **Sooho Choo**[1], **Xiaotian Xu**[5], **Seung Gyo Jeong**[1], **Jitin Sathish Kumar**[1], **Xiaojia Wang**[5], **Andre Mkhoyan**[1], **Marco Bernardi**[4,*] and **Bharat Jalan**[1,*]

[1] Department of Chemical Engineering and Materials Science, University of Minnesota—Twin Cities, Minneapolis, MN 55455, United States of America
[2] Department of Electrical and Computer Engineering, University of Minnesota—Twin Cities, Minneapolis, MN 55455, United States of America
[3] School of Physics and Astronomy, University of Minnesota—Twin Cities, Minneapolis, MN 55455, United States of America
[4] Department of Applied Physics and Materials Science, and Department of Physics, California Institute of Technology, Pasadena, CA 91125, United States of America
[5] Department of Mechanical Engineering, University of Minnesota, Minneapolis, MN 55455, United States of America
[6] Equally contributed.
[*] Authors to whom any correspondence should be addressed.

E-mail: bjalan@umn.edu and bmarco@caltech.edu

Keywords: anatase TiO_2, electron–phonon diagrammatic Monte Carlo, hybrid MBE, mobility, oxygen vacancy, polaron

Supplementary material for this article is available online

Corresponding editor: Dr Lorna Brigham

Abstract

In complex oxides, charge carriers often couple strongly with lattice vibrations to form polarons—entangled electron–phonon quasiparticles whose transport properties remain difficult to characterize. Experimental access to intrinsic polaronic transport requires ultraclean samples, while theoretical description demands methods beyond low-order perturbation theory. Here, we show a predictive theory–experiment workflow to study polaron transport in complex oxides. Focusing on a prototypical polaronic oxide, anatase TiO_2, we combine growth of high-quality oxygen-vacancy-doped films using hybrid molecular beam epitaxy with a first-principles electron–phonon diagrammatic Monte-Carlo (FEP-DMC) framework recently developed for accurate polaron predictions. Our films exhibit record-high electron mobility for anatase TiO_2, in excellent agreement with FEP-DMC calculations conducted prior to experiment, which predict a room-temperature mobility of 45 ± 15 $\mathrm{cm}^{-2}\,\mathrm{V}^{-1}\,\mathrm{s}^{-1}$ and a mobility-temperature scaling of $\mu \propto T^{-1.9 \pm 0.077}$. Microscopic analysis using scanning transmission electron microscopy and x-ray photoelectron spectroscopy reveals the role of oxygen vacancies in modulating transport at lower temperatures. FEP-DMC further provides quantitative insight into polaron formation energy, phonon cloud distribution, lattice distortion around the polaron, and the polaronic contribution to mobility. Together, these results provide a deeper microscopic understanding of large-polaron transport in a complex oxide and provide the blueprint to characterize other polaronic materials.

1. Introduction

Polarons resulting from strong electron–phonon (e–ph) interactions are commonly found in inorganic materials with polar or ionic bonds. In a simple picture, the electron or hole charge carrier polarizes and distorts the surrounding lattice [1]. This effect can be viewed as the formation of a phonon cloud accompanying the charge carrier. In the limit of strong e–ph interactions, the carrier becomes self-trapped at a lattice site, and transport occurs by thermally activated diffusion [1]. The strength and length scale of the e–ph interactions provide criteria to classify polarons. Large polarons are spatially delocalized and originate from long-range e–ph interactions, while small (self-localized) polarons form in the presence of strong, short-range e–ph interactions [1]. Polarons govern the spectral and transport properties in complex oxides [2], and thus a deeper understanding of polaron effects is important in materials physics. In particular, charge transport in polaronic materials can occur through a range of mechanisms, which have been studied extensively using model Hamiltonians, and more recently first-principles calculations [1], but are difficult to predict in real materials.

Among polaronic oxides, titanium dioxide (TiO_2) has attracted attention due to its wide band gap [3, 4], chemical stability [3, 5], optical absorption [6–8], and (photo)catalytic properties [9–13]. TiO_2 has three different polymorphs: rutile, anatase, and brookite [6, 14]. Anatase TiO_2 is a transparent conducting oxide that is known to exhibit pronounced polaron effects, as evidenced by the presence of broadened quasiparticle peaks accompanied by phonon satellites in angle-resolved photoemission spectroscopy (ARPES) spectra [15]. Here, we use anatase TiO_2 as a prototypical oxide to show a combined theory–experiment approach for precise characterization of polaronic transport in the intrinsic, phonon-limited regime. This development is made possible by a combination of advances, respectively, in calculations of strong e–ph interactions and growth of high-quality oxide thin films.

A unified formalism to study e–ph interactions ranging from weak to strong is essential to model transport in polaronic materials [1]. First-principles calculations using the conventional Boltzmann transport equation (BTE) approach are limited to materials with weak e–ph interactions, where electron spectral functions exhibit sharp quasiparticle peaks and polarons are absent [16, 17]. Some of us have recently developed the first-principles e–ph diagrammatic Monte-Carlo (FEP-DMC) method, which quantitatively sums e–ph Feynman diagrams to all orders using material-specific e–ph interactions computed from first principles [18]. FEP-DMC can make accurate predictions of charge transport for both small and large polarons in a unified framework [18]. In parallel, hybrid molecular beam epitaxy (MBE) has emerged as a key approach for atomically-precise synthesis of oxides with low defect density [19]. For Ti-based oxides, growth by conventional oxide MBE is fundamentally constrained by the low vapor pressure of elemental Ti and its strong chemical reactivity with crucible materials, which together limit flux stability and scalability when using solid Ti sources in effusion cells. These limitations are further exacerbated under oxidizing growth conditions, where source surface oxidation can lead to time-dependent flux drift and reduced reproducibility [20, 21]. Despite these challenges, high-quality anatase TiO_2 thin films have been demonstrated using conventional MBE [22, 23]. In contrast, hybrid MBE overcomes these constraints by employing volatile metal–organic Ti precursors, enabling stable and reproducible flux control in oxygen-rich environments and over extended growth times. In this work, we leverage these advantages to grow anatase $TiO_{2\text{-}\delta}$ thin films by hybrid MBE and carry out a systematic investigation of their structural and electrical properties, with particular emphasis on polaronic transport.

Our mobility measurements demonstrate the scaling behavior between mobility μ and temperature as $\mu \propto T^{-1.993 \pm 0.048}$, in remarkable agreement with our FEP-DMC predictions—made prior to experiment—which point to the presence of large polarons with Fröhlich character and a dominant coupling with optical phonons. These results underscore both the accuracy of the theoretical framework and the exceptional quality of the films. Oxygen vacancies act as intrinsic n-type dopants, supplying the carriers that enable transport in this system. By uniting predictive FEP-DMC calculations with hybrid MBE growth and quantitative transport measurements, our work establishes a general framework for microscopic understanding of polaronic charge transport. This combined theory–experiment strategy opens new avenues for unraveling and engineering polaronic phenomena across complex oxides and other quantum materials. Building on the FEP-DMC framework, we introduce the e–ph correlation function, which provides a real-space picture of the polaron and accurately quantifies the polaron lattice distortion and size. Furthermore, experimental transport measurements reveal an evolution of transport behaviors with changing growth conditions, which can be attributed to the oxygen-vacancy ordering in reduced anatase TiO_2 thin films. These observations advance the understanding of polarons and transport properties in anatase TiO_2.

2. Results and discussion

Anatase TiO_2 (tetragonal, $a = b = 3.78$ Å, $c = 9.51$ Å) can be grown epitaxially on $LaAlO_3$ (001) due to the pseudocubic structure of $LaAlO_3$ (001) (pseudocubic lattice parameter = 3.79 Å) and the small in-plane lattice mismatch of −0.2% [24, 25]. Details of the growth process are provided in the Methods section. A metal–organic precursor, titanium tetraisopropoxide (TTIP), is used to supply both Ti and

O and no additional oxygen source is used [21, 26]. This is done deliberately to create oxygen vacancies in films to provide *n*-type carriers and induce conductivity. In figure 1(A), the high-resolution x-ray diffraction (HRXRD) 2θ–ω coupled scans of films grown at four different substrate temperatures ($T_{\mathrm{sub}} = 500$ °C, 600 °C, 700 °C, 900 °C) show that the $\mathrm{TiO}_{2-\delta}$ films exhibit phase-pure anatase structures. Wide-angle scans of these films are shown in figure S1(A). The inset in figure 1(A) shows the film thickness extracted from x-ray reflectivity (XRR) measurements as a function of T_{sub}, where the film thickness increases and stabilizes with increasing substrate temperature. The trend of such T_{sub}-dependent growth rate is similar to that of rutile TiO_2 films grown by hybrid MBE [21]. Figure 1(B) shows the *in-situ* reflection high-energy electron diffraction (RHEED) patterns along the $[100]_{\mathrm{sub}}$ azimuthal direction after growth. The RHEED patterns are spotty when $T_{\mathrm{sub}} = 500$ °C and 600 °C, and become streaky when T_{sub} is increased to 700 °C and 900 °C, suggesting different growth modes in these two temperature regimes [21]. The streaky RHEED patterns at $T_{\mathrm{sub}} \geqslant 700$ °C also indicate smooth surface morphology consistent with the surface step terraces in atomic force microscopy (AFM) and low root-mean square surface roughness as shown in the inset of figure 1(E). At $T_{\mathrm{sub}} \geqslant 700$ °C, RHEED images show a clear ¼ order diffraction peaks (marked by arrows in figure 1(B)), which agrees with the previous studies [22, 24, 27, 28]. We further show the measured room-temperature Hall mobility $\mu_{300\mathrm{K}}$ as a function of growth temperatures in figure S1(B) along with the AFM images on these samples.

We also perform thermal conductivity measurements to characterize the structural quality of our films using time-domain thermoreflectance (TDTR). Figure 1(C) shows TDTR data for a representative 345 nm anatase TiO_2 film grown at 700 °C for 5 h. To eliminate growth-induced oxygen vacancy defects, we anneal the film at 700 °C for 2 h in an oxygen-rich atmosphere using a furnace. The annealed sample exhibits a two-terminal resistance exceeding 200 MΩ, confirming negligible oxygen vacancy concentration. The through-plane thermal conductivity (Λ_z) of the 345 nm anatase TiO_2 film is 4.3 ± 0.4 W m^{-1} $\mathrm{K}^{-1,}$ comparable to reported values for bulk anatase single crystals along the [001] direction [29, 30]. The in-plane thermal conductivity is determined using the beam-offset TDTR method (figure S2), yielding $\Lambda_x \approx \Lambda_y = \Lambda_r = 13.9 \pm 5.4$ W m^{-1} K^{-1}. These results are consistent with prior calculations [29] and highlight a pronounced anisotropy between in-plane and out-of-plane thermal transport, reflecting the anisotropic crystal structure of anatase TiO_2.

To characterize the electronic transport, we introduce oxygen vacancies as intrinsic *n*-type dopants by performing an *in situ* post-growth vacuum annealing at $T_{\mathrm{sub}} = 900$ °C for 15 min. The thermal profile during growth and annealing is illustrated in figure 1(D). Structural characterization by RHEED (inset, figure 1(D), HRXRD (figure 1(E)) confirms that the resulting anatase $\mathrm{TiO}_{2-\delta}$ films are phase-pure, epitaxial, and atomically smooth. A leftward shift of the film peak in XRD further indicates an increased oxygen-vacancy concentration accompanied by an expanded out-of-plane lattice parameter. Temperature-dependent Hall measurements using the van der Pauw geometry are then carried out to probe transport properties. The results, shown in figures S3(A)–(C), include the carrier density $n_{3\mathrm{D}}$, Hall mobility μ, and antisymmetrized Hall resistance R_{xy} as a function of magnetic field B. The negative slopes in R_{xy} confirm *n*-type conduction due to oxygen vacancies, while no measurable conduction is observed in the substrates.

Across all films, the electron mobility follows a scaling relation $\mu \propto T^{\alpha}$. A representative μ vs. T curve (figure 2) shows very close agreement with FEP-DMC theoretical predictions conducted prior to the transport measurements. For context, mobility data from previous experimental studies [31–34] are also plotted. Across the full temperature range, hybrid MBE-grown films exhibit record-high electron mobilities—reaching 31 $\mathrm{cm}^{-2}\,\mathrm{V}^{-1}\,\mathrm{s}^{-1}$ at 300 K and 65 $\mathrm{cm}^{2}\,\mathrm{V}^{-1}\,\mathrm{s}^{-1}$ at 200 K—approaching the phonon-limited lower bound predicted by FEP-DMC (27.5 $\mathrm{cm}^{2}\,\mathrm{V}^{-1}\,\mathrm{s}^{-1}$ at 300 K and 70.2 $\mathrm{cm}^{2}\,\mathrm{V}^{-1}\,\mathrm{s}^{-1}$ at 200 K). This demonstrates that, even in the presence of oxygen vacancies, charge transport is primarily limited by phonon scattering at $T \geqslant 200$ K. Data below 200 K are excluded due to contributions from the Kondo effect which is discussed in the following. Power-law analysis reveals a temperature trend $\mu \propto T^{\alpha}$, with $\alpha = -1.993 \pm 0.048$, in excellent agreement with the FEP-DMC prediction ($\alpha = -1.900 \pm 0.077$). This power-law temperature dependence is a distinctive feature of band-like large polaron transport, similar to the transport regime in SrTiO_3 [17]. Importantly, FEP-DMC calculations identify longitudinal optical (LO) phonons as the dominant scattering channel via the Fröhlich interaction (figures S4(A)–(B)). Furthermore, unlike the conventional BTE, which systematically overestimates the mobility by neglecting polaronic effects, FEP-DMC incorporates higher-order e-ph interactions governing polaronic behavior and reproduces both the magnitude and temperature dependence of the experimental mobilities (figure S4(C)). A more detailed discussion of the FEP-DMC calculations is given in section IV in supplementary information.

To investigate the microscopic structure of polarons and to resolve their energy dispersion in anatase TiO_2, figure 3(A) shows the computed FEP-DMC polaron dispersion band structure (orange line). The

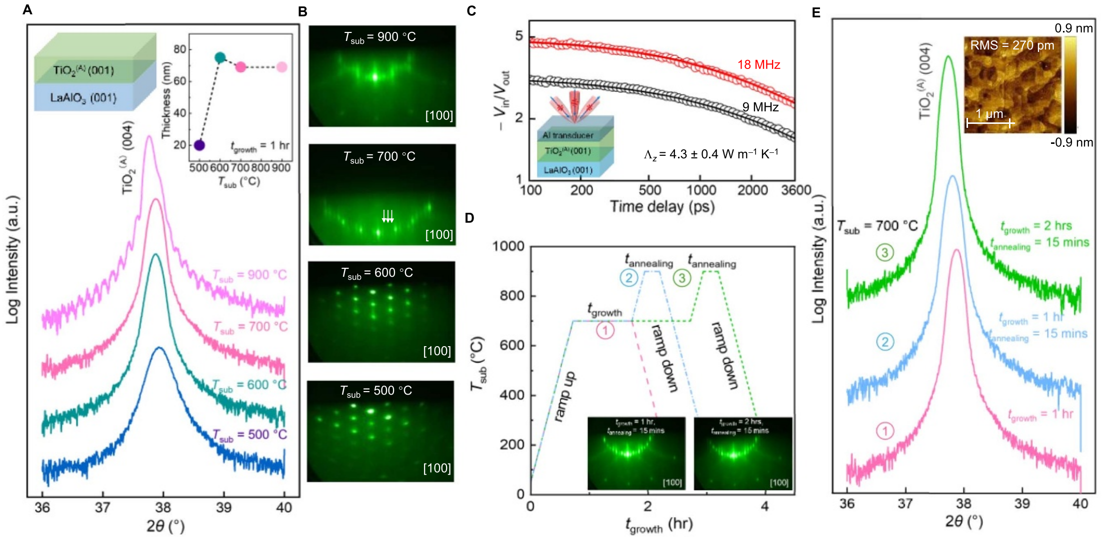

Figure 1. Characterizations of anatase TiO$_{2-\delta}$ films. (A) High resolution x-ray diffraction 2θ–ω coupled scans of TiO$_{2-\delta}^{(A)}$ (001)/LaAlO$_3$ (001) thin films with varying substrate temperatures T_{sub}. The insets show the schematic of the film structure (left) and the thickness of the films as a function of T_{sub}. (B) Reflection high-energy electron diffraction (RHEED) patterns of these thin films with the beam pointing along the [100] direction. (C) Time-domain thermoreflectance ratio (TDTR) signals at room temperature with simultaneous two-frequency fittings on a representative 345 nm film. The inset shows the schematic of the sample structure and the measurement process. (D) Outlines of the growth process and in-situ annealing process. The insets show RHEED patterns for films with the annealing process where the beam points along the [100] direction. (E) High resolution x-ray diffraction 2θ–ω coupled scans of TiO$_{2-\delta}^{(A)}$ (001)/LaAlO$_3$ (001) thin films outlined in (D). The inset shows the atomic force microscopy (AFM) image of the sample 1 outlined in (D) and root mean square (RMS) of the surface roughness.

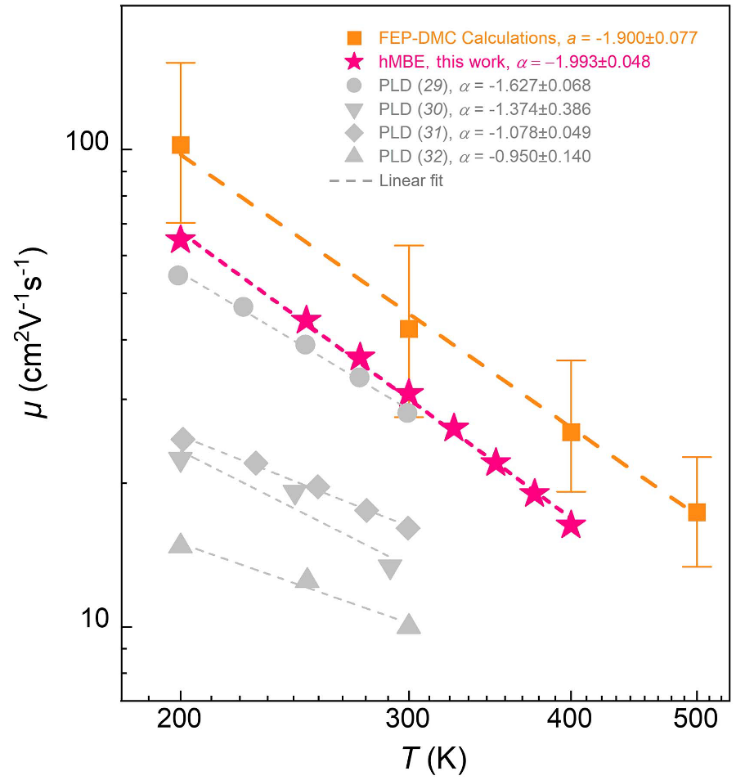

Figure 2. Comparison of carrier mobility in anatase TiO$_2$. Comparison of the computed phonon-limited carrier mobility using the FEP-DMC method (orange squares) with the measured temperature-dependent electron mobility in anatase TiO$_{2-\delta}$ film grown by hybrid MBE (pink stars). Experimental mobility data from previous studies are shown with gray symbols for comparison [31–34]).

G_0W_0 electronic band structure is also shown for comparison (blue line). Energies are referenced to the conduction-band minimum at Γ. The polaron band structure is much flatter than the electronic band structure but is still dispersive, which shows the presence of large polarons in anatase TiO$_2$, whereas

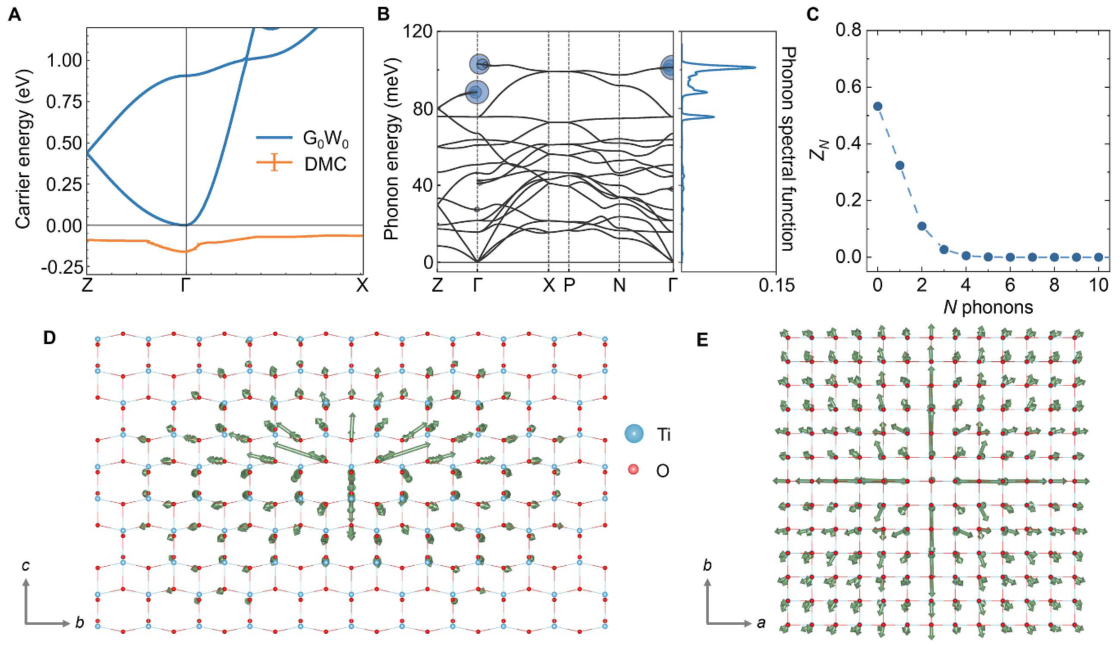

Figure 3. Theoretical modeling of large polarons in anatase TiO_2. (A) Comparison of the computed FEP-DMC polaron dispersion and the G_0W_0 electronic band structure. Energies are referenced to the conduction-band minimum at Γ. The DMC error bars are smaller than the linewidth. (B) The contribution of each phonon mode, Z_Q, in the polaron ground state along high-symmetry lines in the Brillouin zone. The side panel shows the phonon spectral function, $\sum_Q Z_Q \delta(\omega - \omega_Q)$. (C) The phonon number distribution Z_N obtained from the polaron wavefunction. Atomic displacements associated with the polaron, shown for the O atoms in the (D) b–c and (E) a–b planes respectively. The displacements are obtained from the e–ph distortion function defined in the text using FEP-DMC. The length of the arrows is scaled up by 1000 times for visualization purposes.

a dispersion-less band would indicate small polarons [1]. We compute a mass enhancement factor of $m_\mathrm{p}/m_\mathrm{e} = 1.6$ along the Γ–X directions, where m_p is the polaron effective mass and m_e is the electron effective mass, consistent with the value of 1.7 from ARPES measurements [15]. From figure 3(A), we compute the polaron formation energy as the difference between the lowest polaron energy and the lowest electronic energy. Extrapolation to infinite system size gives a polaron formation energy of −0.178 eV, as reported in our previous work [18].

In figure 3(B), we resolve the contribution of each phonon mode to the polaron state, where the marker (solid circle) size is proportional to the amplitude of each phonon mode, Z_Q, in the phonon cloud. This result shows that long-wavelength optical phonons give a dominant contribution, allowing us to classify the polaron in TiO_2 as a Fröhlich-like large polaron formed by the long-range Fröhlich interactions [35]. The side panel, showing the momentum-integrated phonon spectral function, confirms the dominant role of high-energy optical modes. Because the FEP-DMC method returns the complete ground-state polaron wavefunction, we can characterize the phonon number distribution Z_N (figure 3(C)) in the polaron cloud. The rapid decay beyond $N = 3$ shows that on average only a few phonons dress the charge carrier. The zero-phonon amplitude $Z_{N=0}$, which corresponds to the electron quasiparticle weight, is smaller than 1 but remains substantial ($Z_{N=0} \approx 0.6$), underscoring the intermediate-coupling nature of the large polaron. Note that our FEP-DMC transport calculations neglect the phonon-assisted current term; however, a Fermi's-golden-rule estimate shows that its contribution is negligible (see section IV in supplementary information).

The atomic displacements induced by the polaron are typically not evaluated in DMC because this method preserves the translational symmetry [36]. Here, by treating the polaron as a superposition of localized electron and phonon clouds centered at each unit cell, we develop a technique, to be detailed elsewhere, for computing the atomic displacements associated with the polaron in anatase TiO_2. For a many-body polaron wavefunction $|\Phi_0\rangle$, we introduce the e–ph distortion function

$$d_{n,\kappa\alpha}\left(R_p\right) = \left\langle \Phi_0 \left| \sum_{R_i} \hat{c}_n^\dagger\left(R_e\right) \hat{c}_n\left(R_e\right) \hat{u}_{\kappa\alpha}\left(R_p + R_e\right) \right| \Phi_0 \right\rangle$$

which quantifies the displacement of atom κ along direction α at position R_p relative to the center of the electronic Wannier orbital n. We develop an efficient diagrammatic sampling technique to calculate this e–ph distortion function. The resulting atomic displacements are shown in figures 3(D) and (E), in the *b*–*c* and *a*–*b* planes respectively. Because of the large-polaron character, the displacements extend over thousands of unit cells. To characterize the spatial extent of the polaron distortion, we introduce the polaron radius:

$$r_n^{\mathrm{pol}} = \frac{\sum_{\kappa\alpha'} \boldsymbol{R}_p \left|d_{n,\kappa\alpha'}\left(\boldsymbol{R}_p\right)\right|^2 \left|\boldsymbol{R}_p + \tau_\kappa - \tau' n\right|}{\sum_{\kappa\alpha'} \boldsymbol{R}_p \left|d_{n,\kappa\alpha'}\left(\boldsymbol{R}_p\right)\right|^2}$$

where τ_κ and τ'_n are the position of atom κ and the center of Wannier function n within the unit cell respectively. Employing this formula in anatase TiO_2, we obtain $r^{\mathrm{pol}} = 12.9\overset{\circ}{A}$, which is 4.1 times the in-plane lattice constant and is consistent with the size of a large polaron. Interestingly, the lattice perturbation induced by the polaron is more short-ranged along the *c* axis compared to the *a/b* directions, as seen by the more rapid decay of the displacements in the *c* direction. We attribute this anisotropy to the less dispersive band structure along the *c* direction ($\Gamma - Z$ direction in figure 3(A)) compared to the *a*–*b* plane band dispersion ($\Gamma - X$ direction in figure 3(A)). The anisotropic character is particularly important for surface polarons in TiO_2, where the surface termination is expected to impart different polaron energetics and dynamics.

We now turn to the low-temperature electrical transport properties of anatase $TiO_{2-\delta}$ films, focusing on two key features: (1) a pronounced in-plane resistance anisotropy, and (2) an upturn in resistance below ∼200 K. Using 4-terminal van der Pauw measurements (figures S5(A)–(E)) and x-ray photoelectron spectroscopy (XPS) spectroscopy (figure S5(F) and figure S6), we can attribute these features to the Kondo effect induced by the Ti^{3+} states arising from oxygen vacancies (see section V in supplementary information for detailed analysis). Scanning transmission electron microscopy (STEM) provides direct evidence linking oxygen vacancies to the observed transport anisotropy. The low-magnification HAADF-STEM image of a 69 nm $TiO_{2-\delta}/LaAlO_3$ (001) film grown at 700 °C (figure 4(A))–the sample exhibiting large in-plane resistance anisotropy (figure S5(C))–shows non-uniform contrast across the film. An atomic-resolution image of the white-box region (right panel, figure 4(A)) confirms the anatase structure, consistent with HRXRD results. Higher-resolution imaging (figure 4(B)) further reveals spatial variations: some regions display a perfect anatase lattice (rectangle 1, or bottom right corner), while others exhibit alternating dark-bright striping along the $[\bar{2}03]$ direction (rectangle 2, or top left corner), indicative of oxygen-vacancy ordering [37]. Line-scan analysis of HAADF images scanned along the [302] direction i.e. perpendicular to the$[\bar{2}03]$direction (figure 4(C)) further confirms these periodic intensity variations (∼2.1 nm spacing), providing direct evidence of a heterogeneous vacancy distribution. At higher vacancy densities, diffusion across the film homogenizes this distribution, explaining the reduced anisotropy observed at elevated growth temperatures. Collectively, these findings show that both the in-plane anisotropy and the low-temperature resistance upturn in anatase $TiO_{2-\delta}$ films arise from oxygen vacancies—through their density, spatial inhomogeneity, and associated Ti^{3+} states. Future spectroscopy studies will aim to resolve the microscopic origin of the observed contrast.

3. Conclusions

In summary, we demonstrate a unified theory–experiment framework for understanding charge transport in the polaronic regime by combining FEP-DMC calculations and hybrid MBE synthesis of high-quality anatase TiO2-$_\delta$ thin films. Our measurements reveal record-high mobilities and scaling behavior in quantitative agreement with predictions made prior to experiment, highlighting the robustness of FEP-DMC for describing large-polaron transport. Detailed FEP-DMC analysis provides microscopic insight into the polaron state beyond the reach of experiments, including the number and type of phonons in the polaron cloud and the atomic displacements and lattice distortion associated with the polaron. Beyond polaronic conduction, we establish that oxygen vacancies act as intrinsic *n*-type dopants and critically influence low-temperature transport phenomena, including in-plane resistance anisotropy and the Kondo effect. These conclusions are supported by complementary XPS, STEM, and transport measurements, which directly link vacancy density and spatial distribution to anisotropic conduction and magnetic scattering. Together, these results advance the understanding of anatase TiO_2 as a model polaronic system, improve its electronic performance, and introduce a broadly applicable workflow for probing and engineering polaronic transport with atomic resolution in complex oxides and quantum materials.

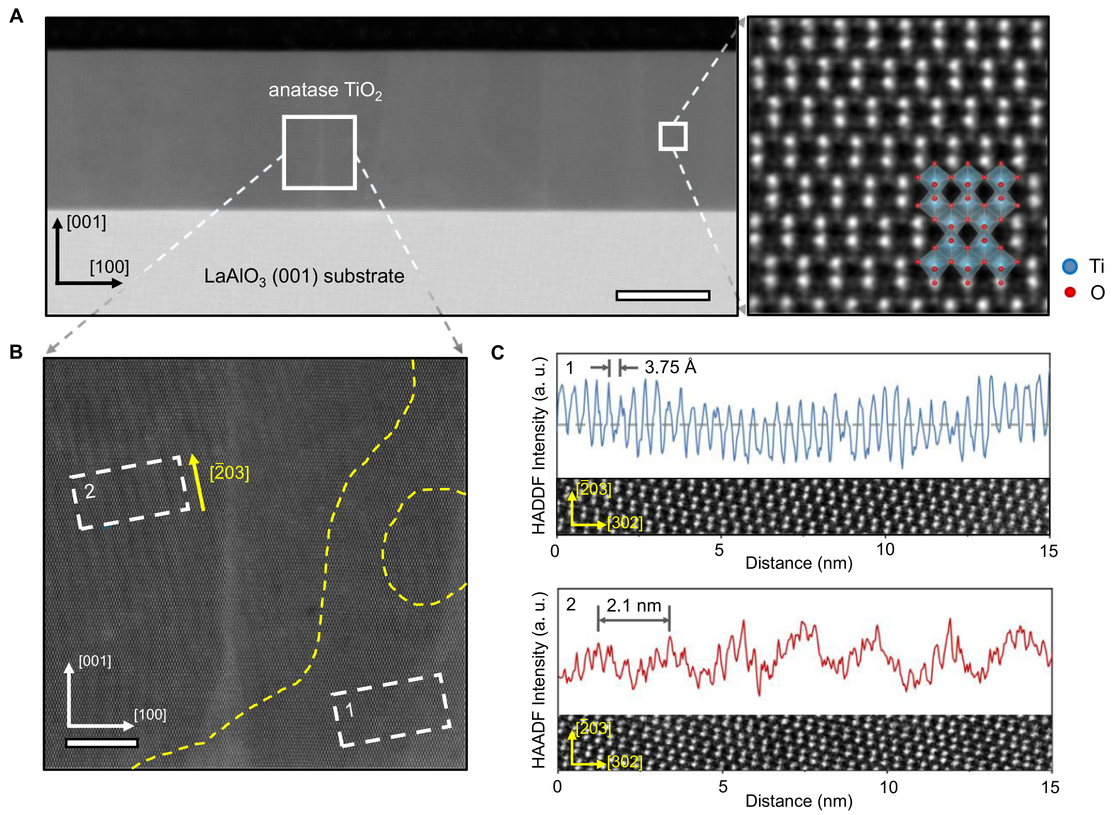

Figure 4. Oxygen vacancies in anatase $TiO_{2-\delta}$ film. (A) Low-magnification HAADF-STEM image of an anatase $TiO_{2-\delta}$ film grown at 700 °C on an $LaAlO_3$ (001) substrate with a thickness of ∼70 nm. The atomic-resolution STEM image of the anatase structure (right) is taken at the white box region. Scale bar = 50 nm. (B) A selected region from the anatase TiO_2 thin film, showing dark-bright strip features along the $[\overline{2}03]$ crystallographic direction. Yellow dashed line marks the boundary between the region with strips and the region with uniform intensity. Scale bar = 10 nm. (C) HAADF intensity line scans from regions 1 and 2 in (B), taken along the [302] direction, i.e. perpendicular to $[\overline{2}03]$ direction. The line scan from region 1 shows a constant average intensity along the grey dashed line, suggesting a uniform region without oxygen vacancies. The inset atomic-resolution image shows the crystal structure of the boxed region. The line scan from region 2 exhibits periodic peaks in addition to the smaller oscillations, where the valleys correspond to dark-strip areas with oxygen vacancies (oxygen deficiencies), while the peaks represent the normal TiO_2 intensity from the bright-strip areas. The spacing between the peaks is approximately 2.1 nm, indicating the distribution of oxygen vacancies. All the images are low-pass filtered for better visualization.

4. Methods

Anatase TiO_2 film growth. All TiO_2 thin films were grown on 5 mm × 5 mm × 0.5 mm $LaAlO_3$ (001) substrates using a hybrid metal–organic MBE approach [21, 26]. Titanium and oxygen were supplied via a metal–organic precursor, titanium tetraisopropoxide (TTIP, 99.999% pure; Sigma-Aldrich). TTIP vapor entered the chamber through a heated gas injector (E-Science, Inc.) in an effusion cell port that was in direct line-of-sight with the substrate. The TTIP vapor reached the injector via a linear leak valve followed by a capacitance manometer (Baratron, MKS Instruments, Inc.), the valve opening serving as the control variable and the manometer pressure serving as the process variable in a control loop. The substrate temperatures were varied from 500 °C to 900 °C. An *in-situ* post-growth annealing was performed at 900 °C for 15 min for some films as outlined in figure 1(D) of the main text.

Film characterization. A Rigaku SmartLab XE diffractometer was used for x-ray diffraction measurements. Film thicknesses were extracted from the XRR. XPS was used to determine the Ti fraction and valence. To determine compositions of the films, XPS fine scans were measured using a Physical Electronics 5000 VersaProbe III photoelectron spectrometer with monochromatic Al $K\alpha$ x-rays, a 55 eV analyzer pass energy, a 50 ms time step and a normal emission geometry. The spectra of C 1*s* and Ti $2p_{3/2}$ were fitted with Lorentzian–Gaussian functions after subtracting the background signal and the C–C peak was calibrated to 284.8 eV. Then the Ti^{3+} contents of the films were determined by calculating the peak area ratios of Ti^{3+} and Ti^{4+}, defined as $A(Ti^{3+})/A(Ti^{3+} + Ti^{4+})$.

Scanning transmission electron microscopy (STEM). The cross-sectional samples for STEM study were prepared using focused ion beam (FIB) (FEI Helios NanoLab G4 dual-beam). A 50 nm of amorphous carbon was first deposited onto the film by thermal evaporation. An additional 2 μm thick amorphous carbon layer was deposited on the region of interest using Ga ion beam to protect this region during FIB milling. The FIB ion beam was operated at 30 kV. STEM imaging was conducted on an aberration-corrected FEI Titan G2 60–300 (S)TEM microscope equipped with a CEOS DCOR probe corrector, monochromator, and a super-X energy dispersive x-ray (EDX) spectrometer. The STEM was operated at a voltage of 200 kV. All the HAADF-STEM images were acquired using a 90 pA probe current. The camera length was set to 130 mm with a probe convergence angle of 25.5 mrad. The HAADF detector's collection angles ranged from 55 mrad to 200 mrad.

Thermal transport measurements. The anisotropic thermal conductivities of a representative anatase TiO_2 film were measured with the ultrafast pump-probe technique, TDTR, along both the through-plane (routine TDTR) and in-plane (beam-offset) directions [38–40]. The TiO_2 film was grown at 700 °C for 5 h, followed by an *ex-situ* furnace annealing at 700 °C for 2 h in an oxygen-rich atmosphere. The film thickness is estimated to be 345 nm based on the calibrated growth rate. Before thermal measurements, a 65 nm Al film was deposited on the TiO_2 film, the $LaAlO_3$ substrate, and a SiO_2 (300 nm)/Si reference sample, serving as the transducer. The thickness of the Al transducer, determined from picosecond acoustics, is consistent for all samples. For routine TDTR measurements of the TiO_2 through-plane thermal conductivity (Λ_z), a 5× objective lens (with a $1/e^2$ radius of $\sim$12 mm) and two modulation frequencies of 9 and 18 MHz were used. The through-plane thermal conductivity of the TiO_2 film was extracted by comparing the experimental data to a 3D heat transfer model [38]. For the in-plane thermal measurements with the beam-offset approach, the TiO_2 film was studied using a 50× objective lens ($1/e^2$ radius of $\sim$1.3 μm) frequency of 1.5 MHz to enhance the measurement sensitivity [39, 41, 42]. The thermal conductivities in two orthogonal in-plane directions (namely, Λ_x and Λ_y) were measured twice for sample loaded at 0° and 90°. The in-plane thermal conductivity is determined by fitting the full width at half maximum of the out-of-phase signal (V_{out}) to the model simulation [41, 43].

Electrical transport measurements. Electrical transport measurements were performed in a Quantum Design Dynacool physical property measurement system in a van der Pauw geometry with aluminum wire bonding to connect samples to the resistivity measurement puck. The temperature range is between 1.8 K and 400 K, and the magnetic field is between ±9 T.

DFT calculations. DFT calculations in anatase TiO_2 employ the Quantum Espresso package with the PBESol exchange-correlation functional [44, 45] and norm-conserving pseudopotentials [46, 47]. We use a plane-wave kinetic energy cutoff of 85 Ry and a lattice parameter $a = 3.78$ Å with the ratio $c/a = 2.51$. We use the Yambo [48] code to compute the G_0W_0 corrected band structure for the lowest 10 conduction bands. The G_0W_0 calculation includes 500 bands to compute the polarization function with the Bruneval–Gonze terminator [49]. We verified that our G_0W_0 band structure in anatase TiO_2 is consistent with previous work [50]. The Wannier functions are constructed using a $6 \times 6 \times 6$ using $\boldsymbol{k}$-point grid with the Wannier90 code [51]. We conduct density functional perturbation theory calculations on a $\boldsymbol{q}$-point grid of $6 \times 6 \times 6$ to compute the lattice dynamics and e–ph perturbation potential, and calculate the e–ph interactions using Perturbo [52].

Acknowledgment

Synthesis (F.L.) is supported primarily by the National Science Foundation (NSF) through the Future of Semiconductor (FuSe) grant under award number DMR-2328702, and under award number DMR-2306273. Transport measurements were supported by the Air Force Office of Scientific Research (AFOSR) through grants FA9550-21-1-0025, and FA9550-23-1-0247. Film growth was performed using instrumentation funded by AFOSR DURIP awards FA9550-18-1-0294 and FA9550-23-1-0085. Part of the work (X-rays spectroscopy) was supported by the U.S. Department of Energy (Award No. DE-SC0020211). Z.Y. acknowledges partial support from the UMN MRSEC program under Award No. DMR-2011401. S.G. and K.A.M. were supported partially by the UMN MRSEC program under Award No. DMR-2011401. This work also benefitted from the AFOSR Multi University Research Initiative (MURI, Award No. FA9550-25-1-0262). Parts of this work were carried out at the Characterization Facility, University of Minnesota, which receives partial support from the NSF through UMN MRSEC. Portions of this work were carried out at the Minnesota Nano Center, which receives support from the NSF through the National Nanotechnology Coordinated Infrastructure (NNCI) under Award No. ECCS-2025124. Y.L. and M.B. were supported by the National Science Foundation under Grant No. OAC-2209262. Y. L. acknowledges support from the Eddleman Fellowship. Thermal studies (C.Z., X.X., and X.W.) were supported by the UMN MRSEC program under Award No. DMR-2011401.

Data statement availability

All data that support the findings of this study are included within the article (and any supplementary files).

Supplementary Information available at http://doi.org/10.1088/1361-6633/ae3c3e/data1.

Conflict of interest

The authors declare no competing interests.

Author contributions

Fengdeng Liu
Conceptualization (equal), Data curation (equal), Formal analysis (equal), Methodology (equal), Validation (equal), Writing – original draft (equal)

Zhifei Yang
Conceptualization (equal), Data curation (equal), Formal analysis (equal), Methodology (equal), Validation (equal), Writing – original draft (equal)

Yao Luo 0000-0001-7026-1271
Conceptualization (equal), Data curation (equal), Formal analysis (equal), Methodology (equal), Validation (equal), Writing – original draft (equal)

Silu Guo
Data curation (supporting), Formal analysis (supporting), Investigation (supporting), Methodology (supporting), Validation (supporting), Writing – review & editing (equal)

Chi Zhang
Data curation (supporting), Formal analysis (supporting), Methodology (supporting), Validation (supporting), Writing – review & editing (supporting)

Sooho Choo 0009-0003-4278-6267
Data curation (supporting), Formal analysis (supporting), Methodology (supporting), Validation (supporting), Writing – review & editing (supporting)

Xiaotian Xu 0009-0000-9246-1223
Data curation (supporting), Formal analysis (supporting), Methodology (supporting), Validation (supporting), Writing – review & editing (supporting)

Seung Gyo Jeong
Formal analysis (supporting), Investigation (supporting), Writing – review & editing (supporting)

Jitin Sathish Kumar
Formal analysis (supporting), Methodology (supporting), Writing – review & editing (supporting)

Xiaojia Wang
Data curation (supporting), Formal analysis (supporting), Funding acquisition (supporting), Investigation (supporting), Methodology (supporting), Project administration (supporting), Supervision (supporting), Validation (supporting), Writing – review & editing (supporting)

Andre Mkhoyan
Data curation (supporting), Formal analysis (supporting), Funding acquisition (supporting), Methodology (supporting), Project administration (supporting), Supervision (supporting), Validation (supporting), Writing – review & editing (supporting)

Marco Bernardi 0000-0001-7289-9666
Conceptualization (equal), Data curation (equal), Formal analysis (equal), Funding acquisition (equal), Investigation (equal), Methodology (equal), Project administration (equal), Supervision (equal), Validation (equal), Writing – original draft (equal)

Bharat Jalan 0000-0002-7940-0490
Conceptualization (equal), Data curation (equal), Formal analysis (equal), Funding acquisition (equal), Investigation (equal), Methodology (equal), Project administration (equal), Supervision (equal), Validation (equal), Writing – original draft (equal)

References

[1] Franchini C, Reticcioli M, Setvin M and Diebold U 2021 Polarons in materials *Nat. Rev. Mater.* **6** 560–86

[2] Chang B K, Timrov I, Park J, Zhou J-J, Marzari N and Bernardi M 2025 First-principles electron-phonon interactions and polarons in the parent cuprate La_2CuO_4 *Phys. Rev. Res.* **7** L012073

[3] Kavan L, Grätzel M, Gilbert S, Klemenz C and Scheel H 1996 Electrochemical and photoelectrochemical investigation of single-crystal anatase *J. Am. Chem. Soc.* **118** 6716–23

[4] Scanlon D O, Dunnill C W, Buckeridge J, Shevlin S A, Logsdail A J, Woodley S M, Catlow C R A, Powell M J, Palgrave R G and Parkin I P 2013 Band alignment of rutile and anatase TiO_2 *Nat. Mater.* **12** 798–801

[5] Rahimi N, Pax R A and Gray E M 2016 Review of functional titanium oxides. I: TiO_2 and its modifications *Prog. Solid State Chem.* **44** 86–105

[6] Carp O, Huisman C L and Reller A 2004 Photoinduced reactivity of titanium dioxide *Prog. Solid State Chem.* **32** 33–177

[7] Wang R, Hashimoto K, Fujishima A, Chikuni M, Kojima E, Kitamura A, Shimohigoshi M and Watanabe T 1998 Photogeneration of highly amphiphilic TiO_2 surfaces *Adv. Mater.* **10** 135–8

[8] O'Regan B and Grätzel M 1991 A low-cost, high-efficiency solar cell based on dye-sensitized colloidal TiO_2 films *Nature* **353** 737–40

[9] Chen J, Ding Z, Wang C, Hou H, Zhang Y, Wang C, Zou G and Ji X 2016 Black anatase titania with ultrafast sodium-storage performances stimulated by oxygen vacancies *ACS. Appl. Mater. Interfaces* **8** 9142–51

[10] Reyes-Coronado D, Rodríguez-Gattorno G, Espinosa-Pesqueira M, Cab C, De Coss R and Oskam G 2008 Phase-pure TiO_2 nanoparticles: anatase, brookite and rutile *Nanotechnology* **19** 145605

[11] Dholam R, Patel N, Adami M and Miotello A 2009 Hydrogen production by photocatalytic water-splitting using Cr-or Fe-doped TiO_2 composite thin films photocatalyst *Int. J. Hydrog. Energy* **34** 5337–46

[12] Peng C *et al* 2022 Regulation of the rutile/anatase TiO_2 phase junction *in-situ* grown on–OH terminated $Ti_3C_2T_x$ (MXene) towards remarkably enhanced photocatalytic hydrogen evolution *Chem. Eng. J.* **439** 135685

[13] Zhang X, Zhu Z, Rao R, Chen J, Han X, Jiang S, Yang Y, Wang Y and Wang L 2023 Highly efficient visible-light-driven photocatalytic degradation of gaseous toluene by rutile-anatase TiO_2@ MIL-101 composite with two heterojunctions *J. Environ. Sci.* **134** 21–33

[14] Hu Y, Tsai H-L and Huang C-L 2003 Effect of brookite phase on the anatase–rutile transition in titania nanoparticles *J. Eur. Ceram. Soc.* **23** 691–6

[15] Moser S, Moreschini L, Jaćimović J, Barišić O, Berger H, Magrez A, Chang Y, Kim K, Bostwick A and Rotenberg E 2013 Tunable polaronic conduction in anatase TiO_2 *Phys. Rev. Lett.* **110** 196403

[16] Kang Y, Peelaers H and Van de Walle C G 2019 First-principles study of electron-phonon interactions and transport in anatase TiO_2 *Phys. Rev. B* **100** 121113

[17] Zhou J-J and Bernardi M 2019 Predicting charge transport in the presence of polarons: the beyond-quasiparticle regime in $SrTiO_3$ *Phys. Rev. Res.* **1** 033138

[18] Luo Y, Park J and Bernardi M 2025 First-principles diagrammatic Monte Carlo for electron-phonon interactions and polaron *Nat. Phys.* **21** 1275–82

[19] Choudhary R and Jalan B 2025 Atomically precise synthesis of oxides with hybrid molecular beam epitaxy *Device* **3** 100711

[20] Theis C D and Schlom D G 1996 Cheap and stable titanium source for use in oxide molecular beam epitaxy systems *J. Vac. Sci. Technol. A* **14** 2677–9

[21] Jalan B, Engel-Herbert R, Cagnon J and Stemmer S 2009 Growth modes in metal-organic molecular beam epitaxy of TiO_2 on r-plane sapphire *J. Vac. Sci. Technol. A* **27** 230–3

[22] Liang Y, Gan S, Chambers S A and Altman E I 2001 Surface structure of anatase TiO_2 (001): reconstruction, atomic steps, and domains *Phys. Rev. B* **63** 235402

[23] Chambers S A, Wang C M, Thevuthasan S, Droubay T, McCready D E, Lea A S, Shutthanandan V and Windisch Jr J C F 2002 Epitaxial growth and properties of MBE-grown ferromagnetic Co-doped TiO_2 anatase films on $SrTiO_3$(001) and $LaAlO_3$(001) *Thin Solid Films* **418** 197–210

[24] Minohara M *et al* 2014 Atomically engineered metal–insulator transition at the TiO_2/$LaAlO_3$ heterointerface *Nano Lett.* **14** 6743–6

[25] Murakami M, Matsumoto Y, Nakajima K, Makino T, Segawa Y, Chikyow T, Ahmet P, Kawasaki M and Koinuma H 2001 Anatase TiO_2 thin films grown on lattice-matched $LaAlO_3$ substrate by laser molecular-beam epitaxy *Appl. Phys. Lett.* **78** 2664–6

[26] Jalan B, Engel-Herbert R, Wright N J and Stemmer S 2009 Growth of high-quality $SrTiO_3$ films using a hybrid molecular beam epitaxy approach *J. Vac. Sci. Technol. A* **27** 461–4

[27] Hengerer R, Bolliger B, Erbudak M and Grätzel M 2000 Structure and stability of the anatase TiO_2 (101) and (001) surfaces *Surf. Sci.* **460** 162–9

[28] Herman G, Sievers M and Gao Y 2000 Structure determination of the two-domain (1× 4) anatase TiO_2 (001) surface *Phys. Rev. Lett.* **84** 3354

[29] Torres P and Rurali R 2019 Thermal conductivity of rutile and anatase TiO_2 from first-principles *J. Phys. Chem. C* **123** 30851–5

[30] Mettan X, Jaćimović J, Barišić O-S, Pisoni A, Batistić I, Horváth E, Brown S, Rossi L, Szirmai P and Farkas B 2019 Tailoring thermal conduction in anatase TiO_2 *Commun. Phys.* **2** 123

[31] Furubayashi Y, Hitosugi T, Yamamoto Y, Inaba K, Kinoda G, Hirose Y, Shimada T and Hasegawa T 2005 A transparent metal: Nb-doped anatase TiO_2 *Appl. Phys. Lett.* **86** 252101

[32] Han Y-L, Luo Z-Z, Li C-J, Shen S-C, Qu G-L, Xiong C-M, Dou R-F, He L and Nie J-C 2014 Carrier-mediated Kondo effect and Hall mobility by electrolyte gating in slightly doped anatase TiO_2 films *Phys. Rev. B* **90** 205107

[33] Krasienapibal T S, Fukumura T, Hirose Y and Hasegawa T 2014 Improved room temperature electron mobility in self-buffered anatase TiO_2 epitaxial thin film grown at low temperature *Japan. J. Appl. Phys.* **53** 090305

[34] Takahashi K and Hwang H 2008 Carrier doping in anatase TiO_2 film by perovskite overlayer deposition *Appl. Phys. Lett.* **93** 082112

[35] Fröhlich H 1954 Electrons in lattice fields *Adv. Phys.* **3** 325–61

[36] Mishchenko A S, Prokof'ev N V, Sakamoto A and Svistunov B V 2000 Diagrammatic quantum Monte Carlo study of the Frohlich polaron *Phys. Rev. B* **62** 6317–36

[37] Knez D, Dražić G, Chaluvadi S K, Orgiani P, Fabris S, Panaccione G, Rossi G and Ciancio R 2020 Unveiling oxygen vacancy superstructures in reduced anatase thin films *Nano Lett.* **20** 6444–51

[38] Cahill D G 2004 Analysis of heat flow in layered structures for time-domain thermoreflectance *Rev. Sci. Instrum.* **75** 5119–22

[39] Zhu J, Park H, Chen J Y, Gu X, Zhang H, Karthikeyan S, Wendel N, Campbell S A, Dawber M and Du X 2016 Revealing the origins of 3D anisotropic thermal conductivities of black phosphorus *Adv. Electron. Mater.* **2** 1600040

[40] Zhang C, Liu F, Guo S, Zhang Y, Xu X, Mkhoyan K A, Jalan B and Wang X 2023 Temperature-dependent thermal conductivity of MBE-grown epitaxial $SrSnO_3$ films *Appl. Phys. Lett.* **123** 042201

[41] Feser J P and Cahill D G 2012 Probing anisotropic heat transport using time-domain thermoreflectance with offset laser spots *Rev. Sci. Instrum.* **83** 104901

[42] Feser J P, Liu J and Cahill D G 2014 Pump-probe measurements of the thermal conductivity tensor for materials lacking in-plane symmetry *Rev. Sci. Instrum.* **85** 104903

[43] Feng T, Wu X, Yang X, Wang P, Zhang L, Du X, Wang X and Pantelides S T 2020 Thermal conductivity of $HfTe_5$: a critical revisit *Adv. Funct. Mater.* **30** 1907286

[44] Perdew J P, Ruzsinszky A, Csonka G I, Vydrov O A, Scuseria G E, Constantin L A, Zhou X and Burke K 2008 Restoring the density-gradient expansion for exchange in solids and surfaces *Phys. Rev. Lett.* **100** 136406

[45] Perdew J P, Burke K and Ernzerhof M 1996 Generalized gradient approximation made simple *Phys. Rev. Lett.* **77** 3865

[46] Hamann D 2013 Optimized norm-conserving Vanderbilt pseudopotentials *Phys. Rev. B* **88** 085117

[47] Perdew J P and Wang Y 1992 Accurate and simple analytic representation of the electron-gas correlation energy *Phys. Rev. B* **45** 13244

[48] Sangalli D, Ferretti A, Miranda H, Attaccalite C, Marri I, Cannuccia E, Melo P, Marsili M, Paleari F and Marrazzo A 2019 Many-body perturbation theory calculations using the Yambo code *J. Phys.: Condens. Matter* **31** 325902

[49] Bruneval F and Gonze X 2008 Accurate GW self-energies in a plane-wave basis using only a few empty states: towards large systems *Phys. Rev. B* **78** 085125

[50] Baldini E, Chiodo L, Dominguez A, Palummo M, Moser S, Yazdi-Rizi M, Auböck G, Mallett B P, Berger H and Magrez A 2017 Strongly bound excitons in anatase TiO_2 single crystals and nanoparticles *Nat. Commun.* **8** 13

[51] Pizzi G, Vitale V, Arita R, Blügel S, Freimuth F, Géranton G, Gibertini M, Gresch D, Johnson C and Koretsune T 2020 Wannier90 as a community code: new features and applications *J. Phys.: Condens. Matter* **32** 165902

[52] Zhou J-J, Park J, Lu I-T, Maliyov I, Tong X and Bernardi M 2021 Perturbo: a software package for ab initio electron–phonon interactions, charge transport and ultrafast dynamics *Comput. Phys. Commun.* **264** 107970